Journal of Mathematics in Industry (2011) 1:2
DOI 10.1186/2190-5983-1-2

Journal of Mathematics in Industry
a SpringerOpen Journal

RESERACH Open Access

Fluid-fiber-interactions in rotational spinning process of glass wool production

Walter Arne · Nicole Marheineke · Johannes Schnebele · Raimund Wegener

Received: 9 December 2010 / Accepted: 3 June 2011 / Published online: 3 June 2011

Abstract The optimal design of rotational production processes for glass wool manufacturing poses severe computational challenges to mathematicians, natural scientists and engineers. In this paper we focus exclusively on the spinning regime where thousands of viscous thermal glass jets are formed by fast air streams. Homogeneity and slenderness of the spun fibers are the quality features of the final fabric. Their prediction requires the computation of the fluid-fiber-interactions which involves the solving of a complex three-dimensional multiphase problem with appropriate interface conditions. But this is practically impossible due to the needed high resolution and adaptive grid refinement. Therefore, we propose an asymptotic coupling concept. Treating the glass jets as viscous thermal Cosserat rods, we tackle the multiscale problem by help of momentum (drag) and heat exchange models that are derived on basis of slender-body theory and homogenization. A weak iterative coupling algorithm that is based on the combination of commercial software and self-implemented code for

W Arne · J Schnebele · R Wegener
Fraunhofer Institut für Techno- und Wirtschaftsmathematik, Fraunhofer Platz 1, D-67663 Kaiserslautern, Germany

J Schnebele
e-mail: johannes.schnebele@itwm.fraunhofer.de

R Wegener
e-mail: raimund.wegener@itwm.fraunhofer.de

W Arne
Fachbereich Mathematik und Naturwissenschaften, Universität Kassel, Heinrich Plett Str. 40, D-34132 Kassel, Germany
e-mail: arne@mathematik.uni-kassel.de

N Marheineke (✉)
FAU Erlangen-Nürnberg, Lehrstuhl Angewandte Mathematik 1, Martensstr. 3, D-91058 Erlangen, Germany
e-mail: marheineke@am.uni-erlangen.de

flow and rod solvers, respectively, makes then the simulation of the industrial process possible. For the boundary value problem of the rod we particularly suggest an adapted collocation-continuation method. Consequently, this work establishes a promising basis for future optimization strategies.

Keywords Rotational spinning process · viscous thermal jets · fluid-fiber interactions · two-way coupling · slender-body theory · Cosserat rods · drag models · boundary value problem · continuation method

Mathematics Subject Classification 76-xx · 34B08 · 41A60 · 65L10 · 65Z05

1 Introduction

Glass wool manufacturing requires a rigorous understanding of the rotational spinning of viscous thermal jets exposed to aerodynamic forces. Rotational spinning processes consist in general of two regimes: melting and spinning. The plant of our industrial partner, Woltz GmbH in Wertheim, is illustrated in Figures 1 and 2. Glass is heated upto temperatures of 1,050°C in a stove from which the melt is led to a centrifugal disk. The walls of the disk are perforated by 35 rows over height with 770 equidistantly placed small holes per row. Emerging from the rotating disk *via* continuous extrusion, the liquid jets grow and move due to viscosity, surface tension, gravity and aerodynamic forces. There are in particular two different air flows that interact with the arising glass fiber curtain: a downwards-directed hot burner flow of 1,500°C that keeps the jets near the nozzles warm and thus extremely viscous and shapeable as well as a highly turbulent cross-stream of 30°C that stretches and finally cools them down such that the glass fibers become hardened. Laying down onto a conveyor belt they yield the basic fabric for the final glass wool product. For the quality assessment of the fabrics the properties of the single spun fibers, that is, homogeneity and slenderness, play an important role. A long-term objective in industry is the optimal design of the manufacturing process with respect to desired product specifications and low production costs. Therefore, it is necessary to model, simulate and control the whole process.

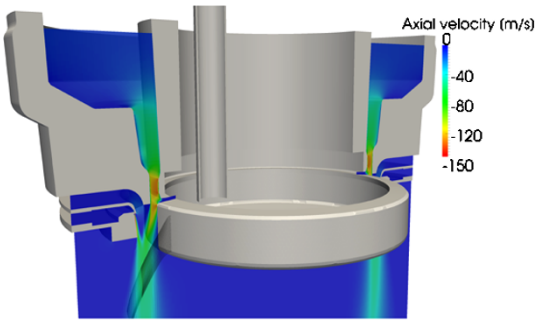

Fig. 1 Rotational spinning process of the company Woltz GmbH, sketch of set-up. Several glass jets forming part of the row-wise arising fiber curtains are shown in the left part of the disc, they are plotted as black curves. The color map visualizes the axial velocity of the air flow. For temperature details see Figure 2.

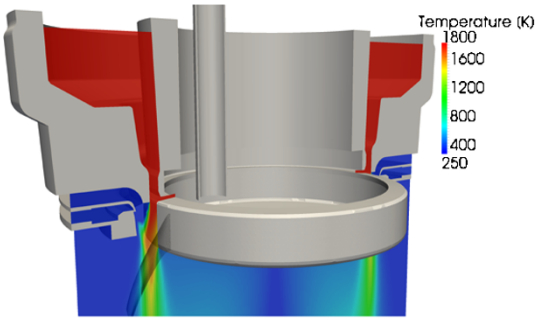

Fig. 2 Rotational spinning process of the company Woltz GmbH, sketch of set-up. Several glass jets forming part of the row-wise arising fiber curtains are shown in the left part of the disc, they are plotted as black curves. The color map visualizes the temperature of air flow. For velocity details see Figure 1.

Up to now, the numerical simulation of the whole manufacturing process is impossible because of its enormous complexity. In fact, we do not long for an uniform numerical treatment of the whole process, but have the idea to derive adequate models and methods for the separate regimes and couple them appropriately, for a similar strategy for technical textiles manufacturing see [1]. In this content, the melting regime dealing with the creeping highly viscous melt flow from the stove to the holes of the centrifugal disk might be certainly handled by standard models and methods from the field of fluid dynamics. It yields the information about the melt velocity and temperature distribution at the nozzles which is of main importance for the ongoing spinning regime. However, be aware that for their determination not only the melt behavior in the centrifugal disk but also the effect of the burner flow, that is, aerodynamic heating and heat distortion of disk walls and nozzles, have to be taken into account. In this paper we assume the conditions at the nozzles to be given and focus exclusively on the spinning regime which is the challenging core of the problem. For an overview of the specific temperature, velocity and length values we refer to Table 1. In the spinning regime the liquid viscous glass jets are formed, in particular they are stretched by a factor 10,000. Their geometry is characterized by a typical slenderness ratio $\delta = d/l \approx 10^{-4}$ of jet diameter d and length l. The resulting fiber properties (characteristics) depend essentially on the jets behavior in the surrounding air flow. To predict them, the interactions, that is, momentum and energy exchange, of air flow and fiber curtain consisting of MN single jets ($M = 35$, $N = 770$) have to be considered. Their computation requires in principle a coupling of fiber jets and flow with appropriate interface conditions. However, the needed high resolution and adap-

Table 1 Typical temperature, velocity and length values in the considered rotational spinning process, cf. Figures 1 and 2.

	Temperature	**Velocity**	**Diameter**
Burner air flow in channel	T_{air1} 1,773 K	V_{air1} $1.2 \cdot 10^2$ m/s	W_1 $1.0 \cdot 10^{-2}$ m
Turbulent air stream at injector	T_{air2} 303 K	V_{air2} $3.0 \cdot 10^2$ m/s	W_2 $2.0 \cdot 10^{-4}$ m
Centrifugal disk	T_{melt} 1,323 K	Ω $2.3 \cdot 10^2$ 1/s	$2R$ $4.0 \cdot 10^{-1}$ m
Glass jets at spinning holes	θ 1,323 K	U $6.7 \cdot 10^{-3}$ m/s	D $7.4 \cdot 10^{-4}$ m

There are $M = 35$ spinning rows, each with $N = 770$ nozzles. The resulting 26,950 glass jets are stretched by a factor 10,000 within the process, their slenderness ratio is $\delta \approx 10^{-4}$.

tive grid refinement make the direct numerical simulation of the three-dimensional multiphase problem for ten thousands of slender glass jets and fast air streams not only extremely costly and complex, but also practically impossible. Therefore, we tackle the multiscale problem by help of drag models that are derived on basis of slender-body theory and homogenization, and a weak iterative coupling algorithm.

The dynamics of curved viscous inertial jets is of interest in many industrial applications (apart from glass wool manufacturing), for example, in nonwoven production [1, 2], pellet manufacturing [3, 4] or jet ink design, and has been subject of numerous theoretical, numerical and experimental investigations, see [5] and references within. In the terminology of [6], there are two classes of asymptotic one-dimensional models for a jet, that is, string and rod models. Whereas the string models consist of balance equations for mass and linear momentum, the more complex rod models contain also an angular momentum balance, [7, 8]. A string model for the jet dynamics was derived in a slender-body asymptotics from the three-dimensional free boundary value problem given by the incompressible Navier-Stokes equations in [5]. Accounting for inner viscous transport, surface tension and placing no restrictions on either the motion or the shape of the jet's center-line, it generalizes the previously developed string models for straight [9–11] and curved [12–14] center-lines. However, already in the stationary case the applicability of the string model turns out to be restricted to certain parameter ranges [15, 16] because of a non-removable singularity that comes from the deduced boundary conditions. These limitations can be overcome by a modification of the boundary conditions, that is, the release of the condition for the jet tangent at the nozzle in favor of an appropriate interface condition, [17–19]. This involves two string models that exclusively differ in the closure conditions. For gravitational spinning scenarios they cover the whole parameter range, but in the presence of rotations there exist small parameter regimes where none of them works. A rod model that allows for stretching, bending and twisting was proposed and analyzed in [20, 21] for the coiling of a viscous jet falling on a rigid substrate. Based on these studies and embedded in the special Cosserat theory a modified incompressible isothermal rod model for rotational spinning was developed and investigated in [16, 19]. It allows for simulations in the whole (Re, Rb, Fr)-range and shows its superiority to the string models. These observations correspond to studies on a fluid-mechanical 'sewing machine', [22, 23]. By containing the slenderness parameter δ explicitely in the angular momentum balance, the rod model is no asymptotic model of zeroth order. Since its solutions converge to the respective string solutions in the slenderness limit $\delta \to 0$, it can be considered as δ-regularized model, [19]. In this paper we extend the rod model by incorporating the practically relevant temperature dependencies and aerodynamic forces. Thereby, we use the air drag model F of [24] that combines Oseen and Stokes theory [25–27], Taylor heuristic [28] and numerical simulations. Being validated with experimental data [29–32], it is applicable for all air flow regimes and incident flow directions. Transferring this strategy, we model a similar aerodynamic heat source for the jet that is based on the Nusselt number Nu [33]. Our coupling between glass jets and air flow follows then the principle that action equals reaction. By inserting the corresponding homogenized source terms induced by F and Nu in the balance equations of the air flow, we make the proper momentum and energy exchange within this slender-body framework possible.

The paper is structured as follows. We start with the general coupling concept for slender bodies and fluid flows. Therefore, we introduce the viscous thermal Cosserat rod system and the compressible Navier-Stokes equations for glass jets and air flow, respectively, and present the models for the momentum and energy exchange: drag F and Nusselt function Nu. The special set-up of the industrial rotational spinning process allows for the simplification of the model framework, that is, transition to stationarity and assumption of rotational invariance as we discuss in detail. It follows the section about the numerical treatment. To realize the fiber-flow interactions we use a weak iterative coupling algorithm, which is adequate for the problem and has the advantage that we can combine commercial software and self-implemented code. Special attention is paid to the collocation and continuation method for solving the boundary value problem of the rod. Convergence of the coupling algorithm and simulation results are shown for a specific spinning adjustment. This illustrates the applicability of our coupling framework as one of the basic tools for the optimal design of the whole manufacturing process. Finally, we conclude with some remarks to the process.

2 General coupling concept for slender bodies and fluid flows

We are interested in the spinning of ten thousands of slender glass jets by fast air streams, $MN = 26{,}950$. The glass jets form a kind of curtain that interact and crucially affect the surrounding air. The determination of the fluid-fiber-interactions requires in principle the simulation of the three-dimensional multiphase problem with appropriate interface conditions. However, regarding the complexity and enormous computational effort, this is practically impossible. Therefore, we propose a coupling concept for slender bodies and fluid flows that is based on drag force and heat exchange models. In this section we first present the two-way coupling of a single viscous thermal Cosserat rod and the compressible Navier-Stokes equations and then generalize the concept to many rods. Thereby, we choose an invariant formulation in the three-dimensional Euclidian space $\mathbb{E}^3$.

Note that we mark all quantities associated to the air flow by the subscript $_\star$ throughout the paper. Moreover, to facilitate the readability of the coupling concept, we introduce the abbreviations $\boldsymbol{\Psi}$ and $\boldsymbol{\Psi}_\star$ that represent all quantities of the glass jets and the air flow, respectively.

2.1 Models for glass jets and air flows

2.1.1 Cosserat rod

A glass jet is a slender body, that is, a rod in the context of three-dimensional continuum mechanics. Because of its slender geometry, its dynamics might be reduced to a one-dimensional description by averaging the underlying balance laws over its cross-sections. This procedure is based on the assumption that the displacement field in each cross-section can be expressed in terms of a finite number of vector- and tensor-valued quantities. In the special Cosserat rod theory, there are only two constitutive

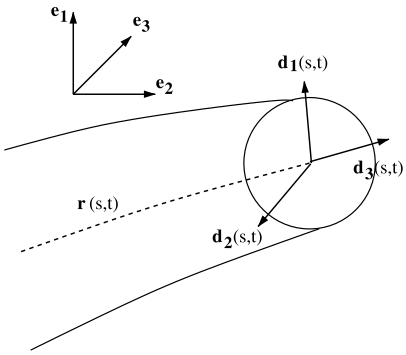

Fig. 3 Special Cosserat rod with Kirchhoff constraint $\partial_s r = \mathbf{d_3}$.

elements: a curve specifying the position $\mathbf{r} : Q \to \mathbb{E}^3$ and an orthonormal director triad $\{\mathbf{d_1}, \mathbf{d_2}, \mathbf{d_3}\} : Q \to \mathbb{E}^3$ characterizing the orientation of the cross-sections, where $Q = \{(s,t) \in \mathbb{R}^2 | s \in I(t) = [0, l(t)], t > 0\}$ with arclength parameter s and time t. For a schematic sketch of a Cosserat rod see Figure 3, for more details on the Cosserat theory we refer to [6]. In the following we use an incompressible viscous Cosserat rod model that was derived on basis of the work [20, 34] on viscous rope coiling and investigated for isothermal curved inertial jets in rotational spinning processes [16, 19]. We extend the model by incorporating temperature effects and aerodynamic forces. The rod system describes the variables of jet curve $\mathbf{r}$, orthonormal triad $\{\mathbf{d_1}, \mathbf{d_2}, \mathbf{d_3}\}$, generalized curvature $\boldsymbol{\kappa}$, convective speed u, cross-section A, linear velocity $\mathbf{v}$, angular velocity $\boldsymbol{\omega}$, temperature T and normal contact forces $\mathbf{n} \cdot \mathbf{d_\alpha}$, $\alpha = 1, 2$. It consists of four kinematic and four dynamic equations, that is, balance laws for mass (cross-section), linear and angular momentum and temperature,

$$\begin{aligned}
\partial_t \mathbf{r} &= \mathbf{v} - u\mathbf{d_3}, \\
\partial_t \mathbf{d_i} &= (\boldsymbol{\omega} - u\boldsymbol{\kappa}) \times \mathbf{d_i}, \\
\partial_s \mathbf{r} &= \mathbf{d_3}, \\
\partial_s \mathbf{d_i} &= \boldsymbol{\kappa} \times \mathbf{d_i}, \\
\partial_t A + \partial_s (uA) &= 0, \\
\rho\big(\partial_t (A\mathbf{v}) + \partial_s (uA\mathbf{v})\big) &= \partial_s \mathbf{n} + \rho A g \mathbf{e_g} + \mathbf{f}_{air}, \\
\rho\big(\partial_t (\mathbf{J} \cdot \boldsymbol{\omega}) + \partial_s (u\mathbf{J} \cdot \boldsymbol{\omega})\big) &= \partial_s \mathbf{m} + \mathbf{d_3} \times \mathbf{n}, \\
\rho c_p\big(\partial_t (AT) + \partial_s (uAT)\big) &= q_{rad} + q_{air}
\end{aligned} \tag{1}$$

supplemented with an incompressible geometrical model of circular cross-sections with diameter d

$$\begin{aligned}
\mathbf{J} &= I(\mathbf{d_1} \otimes \mathbf{d_1} + \mathbf{d_2} \otimes \mathbf{d_2} + 2\mathbf{d_3} \otimes \mathbf{d_3}), \\
I &= \frac{\pi}{64} d^4, \quad A = \frac{\pi}{4} d^2
\end{aligned}$$

as well as viscous material laws for the tangential contact force $\mathbf{n}\cdot\mathbf{d_3}$ and contact couple $\mathbf{m}$

$$\mathbf{n}\cdot\mathbf{d_3} = 3\mu A\partial_s u$$
$$\mathbf{m} = 3\mu I\left(\mathbf{d_1}\otimes\mathbf{d_1} + \mathbf{d_2}\otimes\mathbf{d_2} + \frac{2}{3}\mathbf{d_3}\otimes\mathbf{d_3}\right)\cdot\partial_s\boldsymbol{\omega}.$$

Rod density ρ and heat capacity c_p are assumed to be constant. The temperature-dependent dynamic viscosity μ is modeled according to the Vogel-Fulcher-Tamman relation, that is, $\mu(T) = 10^{p_1+p_2/(T-p_3)}$ Pa s where we use the parameters $p_1 = -2.56$, $p_2 = 4{,}289.18$ K and $p_3 = (150.74+273.15)$ K, [33]. The external loads rise from gravity $\rho A g\mathbf{e_g}$ with gravitational acceleration g and aerodynamic forces $\mathbf{f}_{air}$. In the temperature equation we neglect inner friction and heat conduction and focus exclusively on radiation q_{rad} and aerodynamic heat sources q_{air}. The radiation effect depends on the geometry of the plant and is incorporated in the system by help of the simple model

$$q_{rad} = \varepsilon_R\sigma\pi d\left(T_{ref}^4 - T^4\right)$$

with emissivity ε_R, Stefan-Boltzmann constant σ and reference temperature T_{ref}. Appropriate initial and boundary conditions close the rod system.

2.1.2 Navier-Stokes equations

A compressible air flow in the space-time domain $\Omega_t = \{(\mathbf{x},t)|\mathbf{x}\in\Omega\subset\mathbb{E}^3, t>0\}$ is described by density $\rho_\star$, velocity $\mathbf{v}_\star$, temperature $T_\star$. Its model equations consist of the balance laws for mass, momentum and energy,

$$\begin{aligned}
\partial_t\rho_\star + \nabla\cdot(\mathbf{v}_\star\rho_\star) &= 0,\\
\partial_t(\rho_\star\mathbf{v}_\star) + \nabla\cdot(\mathbf{v}_\star\otimes\rho_\star\mathbf{v}_\star) &= \nabla\cdot\mathbf{S}_\star^T + \rho_\star g\mathbf{e_g} + \mathbf{f}_{jets},\\
\partial_t(\rho_\star e_\star) + \nabla\cdot(\mathbf{v}_\star\rho_\star e_\star) &= \mathbf{S}_\star : \nabla\mathbf{v}_\star - \nabla\cdot\mathbf{q}_\star + q_{jets}
\end{aligned} \tag{2}$$

supplemented with the Newtonian stress tensor $\mathbf{S}_\star$, the Fourier law for heat conduction $\mathbf{q}_\star$

$$\mathbf{S}_\star = -p_\star\mathbf{I} + \mu_\star\left(\nabla\mathbf{v}_\star + \nabla\mathbf{v}_\star^T\right) + \lambda_\star\nabla\cdot\mathbf{v}_\star\mathbf{I},$$
$$\mathbf{q}_\star = -k_\star\nabla T_\star,$$

as well as thermal and caloric equations of state of a ideal gas

$$p_\star = \rho_\star R_\star T_\star, \quad e_\star = \int_0^{T_\star} c_{p\star}(T)\,\mathrm{d}T - \frac{p_\star}{\rho_\star}$$

with pressure $p_\star$ and inner energy $e_\star$. The specific gas constant for air is denoted by $R_\star$. The temperature-dependent viscosities $\mu_\star$, $\lambda_\star$, heat capacity $c_{p\star}$ and heat conductivity $k_\star$ can be modeled by standard polynomial laws, see, for example, [33, 35].

External loads rise from gravity $\rho_\star g \mathbf{e_g}$ and forces due to the immersed fiber jets $\mathbf{f}_{jets}$. These fiber jets also imply a heat source q_{jets} in the energy equation. Appropriate initial and boundary conditions close the system.

2.2 Models for momentum and energy exchange

The coupling of the Cosserat rod and the Navier-Stokes equations is performed by help of drag forces and heat sources. Taking into account the conservation of momentum and energy, $\mathbf{f}_{air}$ and $\mathbf{f}_{jets}$ as well as q_{air} and q_{jets} satisfy the principle that action equals reaction and obey common underlying relations. Hence, we can handle the delicate fluid-fiber-interactions by help of two surrogate models, so-called exchange functions, that is, a dimensionless drag force F (inducing $\mathbf{f}_{air}$, $\mathbf{f}_{jets}$) and Nusselt number Nu (inducing q_{air}, q_{jets}). For a flow around a slender long cylinder with circular cross-sections there exist plenty of theoretical, numerical and experimental investigations to these relations in literature, for an overview see [24] as well as, for example, [29, 30, 33, 36] and references within. We use this knowledge locally and globalize the models by superposition to apply them to our curved moving Cosserat rod. This strategy follows a Global-from-Local concept [37] that turned out to be very satisfying in the derivation and validation of a stochastic drag force in a one-way coupling of fibers in turbulent flows [24].

2.2.1 Drag forces - $\mathbf{f}_{air}$ vs $\mathbf{f}_{jets}$

Let $\boldsymbol{\Psi}$ and $\boldsymbol{\Psi}_\star$ represent all glass jet and air flow quantities, respectively. Thereby, $\boldsymbol{\Psi}_\star$ is the spatially averaged solution of (2). This delocation is necessary to avoid singularities in the two-way coupling. Then, the drag forces are given by

$$\begin{aligned}
\mathbf{f}_{air}(s,t) &= \boldsymbol{\mathcal{F}}\big(\boldsymbol{\Psi}(s,t), \boldsymbol{\Psi}_\star\big(\mathbf{r}(s,t),t\big)\big),\\
\mathbf{f}_{jets}(\mathbf{x},t) &= -\int_{I(t)} \delta\big(\mathbf{x}-\mathbf{r}(s,t)\big)\boldsymbol{\mathcal{F}}\big(\boldsymbol{\Psi}(s,t), \boldsymbol{\Psi}_\star(\mathbf{x},t)\big)\,\mathrm{d}s,\\
\boldsymbol{\mathcal{F}}(\boldsymbol{\Psi},\boldsymbol{\Psi}_\star) &= \frac{\mu_\star^2}{d\rho_\star}\mathbf{F}\left(\mathbf{d_3}, \frac{d\rho_\star}{\mu_\star}(\mathbf{v}_\star-\mathbf{v})\right),
\end{aligned}$$

where δ is the Dirac distribution. By construction, they fulfill the principle that action equals reaction and hence the momentum is conserved, that is,

$$\int_{I_V(t)} \mathbf{f}_{air}(s,t)\,\mathrm{d}s = -\int_V \mathbf{f}_{jets}(\mathbf{x},t)\,\mathrm{d}\mathbf{x}$$

for an arbitrary domain V and $I_V(t) = \{s \in I(t) | \mathbf{r}(s,t) \in V\}$. The (line) force $\boldsymbol{\mathcal{F}}$ acting on a slender body is caused by friction and inertia. It depends on material and geometrical properties as well as on the specific inflow situation. The number of dependencies can be reduced to two by help of non-dimensionalizing which yields the dimensionless drag force $\mathbf{F}$ in dependence on the jet orientation (tangent) and the dimensionless relative velocity between air flow and glass jet. Due to the rotational invariance of the force, the function

$$\mathbf{F} : S^2 \times \mathbb{E}^3 \to \mathbb{E}^3$$

can be associated with its component tuple F for every representation in an orthonormal basis, that is,

$$\mathrm{F}: S^2_{\mathbb{R}^3} \times \mathbb{R}^3 \to \mathbb{R}^3,$$

$$\mathrm{F} = (F_1, F_2, F_3) \quad \text{with} \quad \sum_{i=1}^{3} F_i(\tau, \mathrm{w})\mathbf{e_i} = \mathbf{F}\left(\sum_{i=1}^{3} \tau_i \mathbf{e_i}, \sum_{i=1}^{3} w_i \mathbf{e_i}\right)$$

for every orthonormal basis $\{\mathbf{e_i}\}$.

For F we use the drag model [24] that was developed on top of Oseen and Stokes theory [25–27], Taylor heuristic [28] and numerical simulations and validated with measurements [29–32]. It shows to be applicable for all air flow regimes and incident flow directions. Let $\{\mathbf{n}, \mathbf{b}, \boldsymbol{\tau}\}$ be the orthonormal basis induced by the specific inflow situation $(\boldsymbol{\tau}, \mathbf{w})$ with orientation $\boldsymbol{\tau}$ and velocity $\mathbf{w}$, assuming $\mathbf{w} \nparallel \boldsymbol{\tau}$,

$$\mathbf{n} = \frac{\mathbf{w} - w_\tau \boldsymbol{\tau}}{w_n}, \quad \mathbf{b} = \boldsymbol{\tau} \times \mathbf{n},$$

$$w_\tau = \mathbf{w} \cdot \boldsymbol{\tau}, \quad w_n = \sqrt{\mathbf{w}^2 - w_\tau^2}.$$

Then, the force is given by

$$\begin{aligned} \mathbf{F}(\boldsymbol{\tau}, \mathbf{w}) &= F_n(w_n)\mathbf{n} + F_\tau(w_n, w_\tau)\boldsymbol{\tau}, \\ F_n(w_n) &= w_n^2 c_n(w_n) = w_n r_n(w_n), \\ F_\tau(w_n, w_\tau) &= w_\tau w_n c_\tau(w_n) = w_\tau r_\tau(w_n) \end{aligned} \tag{3}$$

according to the Independence Principle [38]. The differentiable normal and tangential drag functions c_n, c_τ are

$$c_n(w_n) = \begin{cases} \dfrac{4\pi}{S w_n}\left[1 - w_n^2 \dfrac{S^2 - S/2 + 5/16}{32S}\right], & w_n < w_1, \\ \exp\left(\displaystyle\sum_{j=0}^{3} p_{n,j} \ln^j w_n\right), & w_1 \le w_n \le w_2, \\ \dfrac{2}{\sqrt{w_n}} + 0.5, & w_2 < w_n, \end{cases}$$

$$c_\tau(w_n) = \begin{cases} \dfrac{4\pi}{(2S-1) w_n}\left[1 - w_n^2 \dfrac{2S^2 - 2S + 1}{16(2S-1)}\right], & w_n < w_1, \\ \exp\left(\displaystyle\sum_{j=0}^{3} p_{\tau,j} \ln^j w_n\right), & w_1 \le w_n \le w_2, \\ \dfrac{\gamma}{\sqrt{w_n}}, & w_2 < w_n, \end{cases}$$

with $S(w_n) = 2.0022 - \ln w_n$, transition points $w_1 = 0.1$, $w_2 = 100$, amplitude $\gamma = 2$. The regularity involves the parameters $p_{n,0} = 1.6911$, $p_{n,1} = -6.7222 \cdot 10^{-1}$,

$p_{n,2} = 3.3287 \cdot 10^{-2}$, $p_{n,3} = 3.5015 \cdot 10^{-3}$ and $p_{\tau,0} = 1.1552$, $p_{\tau,1} = -6.8479 \cdot 10^{-1}$, $p_{\tau,2} = 1.4884 \cdot 10^{-2}$, $p_{\tau,3} = 7.4966 \cdot 10^{-4}$. To be also applicable in the special case of a transversal incident flow $\mathbf{w} \parallel \boldsymbol{\tau}$ and to ensure a realistic smooth force $\mathbf{F}$, the drag is modified for $w_n \to 0$. A regularization based on the slenderness parameter δ matches the associated resistance functions r_n, r_τ (3) to Stokes resistance coefficients of higher order for $w_n \ll 1$, for details see [24].

2.2.2 *Heat sources - q_{air} vs q_{jets}*

Analogously to the drag forces, the heat sources are given by

$$
\begin{aligned}
q_{air}(s,t) &= \mathcal{Q}\big(\boldsymbol{\Psi}(s,t), \boldsymbol{\Psi}_\star\big(\mathbf{r}(s,t),t\big)\big),\\
q_{jets}(\mathbf{x},t) &= -\int_{I(t)} \delta\big(\mathbf{x}-\mathbf{r}(s,t)\big)\mathcal{Q}\big(\boldsymbol{\Psi}(s,t), \boldsymbol{\Psi}_\star(\mathbf{x},t)\big)\,\mathrm{d}s,\\
\mathcal{Q}(\boldsymbol{\Psi}, \boldsymbol{\Psi}_\star) &= 2k_\star(T_\star - T)\mathrm{Nu}\left(\frac{\mathbf{v}_\star - \mathbf{v}}{\|\mathbf{v}_\star - \mathbf{v}\|}\cdot\mathbf{d_3}, \frac{\pi}{2}\frac{d\rho_\star}{\mu_\star}\|\mathbf{v}_\star - \mathbf{v}\|, \frac{\mu_\star c_{p\star}}{k_\star}\right).
\end{aligned}
$$

The (line) heat source $\mathcal{Q}$ acting on a slender body also depends on several material and geometrical properties as well as on the specific inflow situation. The number of dependencies can be reduced to three by help of non-dimensionalizing which yields the dimensionless Nusselt number Nu in dependence of the cosine of the angle of attack, Reynolds and Prandtl numbers. The Reynolds number corresponds to the relative velocity between air flow and glass jet, the typical length is the half jet circumference.

For Nu we use a heuristic model. It originates in the studies of a perpendicular flow around a cylinder [33] and is modified for different inflow directions (angles of attack) with regard to experimental data. A regularization ensures the smooth limit for a transversal incident flow in analogon to the drag model for F in (3). We apply

$$
\begin{aligned}
&\mathrm{Nu} : [-1,1] \times \mathbb{R}_0^+ \times \mathbb{R}_0^+ \to \mathbb{R}_0^+,\\
&\mathrm{Nu}(c,\mathrm{Re},\mathrm{Pr}) = \big(1 - 0.5h^2(c,\mathrm{Re})\big)\big(0.3 + \sqrt{\mathrm{Nu}_{la}^2(\mathrm{Re},\mathrm{Pr}) + \mathrm{Nu}_{tu}^2(\mathrm{Re},\mathrm{Pr})}\big),\\
&\mathrm{Nu}_{la}(\mathrm{Re},\mathrm{Pr}) = 0.664\mathrm{Re}^{1/2}\mathrm{Pr}^{3/2},\\
&\mathrm{Nu}_{tu}(\mathrm{Re},\mathrm{Pr}) = \frac{0.037\mathrm{Re}^{0.9}\mathrm{Pr}}{\mathrm{Re}^{0.1} + 2.443(\mathrm{Pr}^{2/3}-1)},\\
&h(c,\mathrm{Re}) = \begin{cases} c\mathrm{Re}/\delta_h, & \mathrm{Re} < \delta_h,\\ c, & \mathrm{Re} \geq \delta_h. \end{cases}
\end{aligned}
\tag{4}
$$

2.3 Generalization to many rods

In case of k slender bodies in the air flow, we have $\boldsymbol{\Psi}_\mathbf{i}$, $i = 1, \ldots, k$, representing the quantities of each Cosserat rod, here $k = MN$. Assuming no contact between neighboring fiber jets, every single jet can be described by the stated rod system (1).

Their multiple effect on the air flow is reflected in $\mathbf{f}_{jets}$ and q_{jets}. The source terms in the momentum and energy equations of the air flow (2) become

$$\mathbf{f}_{jets}(\mathbf{x},t) = -\sum_{i=1}^{k} \int_{I_i(t)} \delta\big(\mathbf{x}-\mathbf{r_i}(s,t)\big)\mathcal{F}\big(\mathbf{\Psi_i}(s,t),\mathbf{\Psi}_\star(\mathbf{x},t)\big)\,\mathrm{d}s,$$

$$q_{jets}(\mathbf{x},t) = -\sum_{i=1}^{k} \int_{I_i(t)} \delta\big(\mathbf{x}-\mathbf{r_i}(s,t)\big)\mathcal{Q}\big(\mathbf{\Psi_i}(s,t),\mathbf{\Psi}_\star(\mathbf{x},t)\big)\,\mathrm{d}s.$$

3 Models for special set-up of rotational spinning process

In the rotational spinning process under consideration the centrifugal disk is perforated by M rows of N equidistantly placed holes each ($M = 35$, $N = 770$). The spinning conditions (hole size, velocities, temperatures) are thereby identical for each row, see Figures 1 and 2. The special set-up allows for the simplification of the general model framework. We introduce the rotating outer orthonormal basis $\{\mathbf{a_1}(t), \mathbf{a_2}(t), \mathbf{a_3}(t)\}$ satisfying $\partial_t \mathbf{a_i} = \mathbf{\Omega} \times \mathbf{a_i}$, $i = 1, 2, 3$, where $\mathbf{\Omega}$ is the angular frequency of the centrifugal disk. In particular, $\mathbf{\Omega} = \Omega \mathbf{a_1}$ and $\mathbf{e_g} = -\mathbf{a_1}$ (gravity direction) hold. Then, glass jets and air flow become stationary, presupposing that we consider spun fiber jets of certain length. In particular, we assume the stresses to be vanished at this length. Moreover, the glass jets emerging from the rotating device form dense curtains for every spinning row. As a result of homogenization, we can treat the air flow as rotationally invariant and each curtain can be represented by one jet. This yields an enormous complexity reduction of the problem. The homogenization together with the slender-body theory makes the numerical simulation possible.

3.1 Transition to stationarity

3.1.1 Representative spun jet of certain length

For the viscous Cosserat rods (1), the mass flux Q is constant in the stationarity, that is, $uA = Q/\rho = const$. We deal with $\mathbf{\Omega}$-adapted linear and angular velocities, $\mathbf{v}_\Omega = \mathbf{v} - \mathbf{\Omega} \times \mathbf{r}$ and $\boldsymbol{\omega}_\Omega = \boldsymbol{\omega} - \mathbf{\Omega}$, which fulfill the explicit stationarity relations

$$\mathbf{v}_\Omega = u\mathbf{d_3}, \quad \boldsymbol{\omega}_\Omega = u\boldsymbol{\kappa}$$

resulting from the first two equations of (1). Moreover, fictitious Coriolis and centrifugal forces and associated couples enter the linear and angular momentum equations. Using the material laws we can formulate the stationary rod model in terms of a boundary value problem of first order differential equations. Thereby, we present it in the director basis $\{\mathbf{d_1}, \mathbf{d_2}, \mathbf{d_3}\}$ for convenience (see (5) and compare to [19] except for the temperature equation). Note that to an arbitrary vector field $\mathbf{z} = \sum_{i=1}^{3} \check{z}_i \mathbf{a_i} = \sum_{i=1}^{3} z_i \mathbf{d_i} \in \mathbb{E}^3$, we indicate the component tuples corresponding to the rotating outer basis and the director basis by $\check{\mathsf{z}} = (\check{z}_1, \check{z}_2, \check{z}_3) \in \mathbb{R}^3$ and $\mathsf{z} = (z_1, z_2, z_3) \in \mathbb{R}^3$, respectively. The director basis can be transformed into the rotating outer basis by the

tensor-valued rotation $\mathbf{R}$, that is, $\mathbf{R} = \mathbf{a_i} \otimes \mathbf{d_i} = R_{ij}\mathbf{a_i} \otimes \mathbf{a_j} \in \mathbb{E}^3 \otimes \mathbb{E}^3$ with associated orthogonal matrix $\mathsf{R} = (R_{ij}) = (\mathbf{d_i} \cdot \mathbf{a_j}) \in \mathrm{SO}(3)$. Its transpose and inverse matrix is denoted by R^{T}. For the components, $\mathsf{z} = \mathsf{R} \cdot \check{\mathsf{z}}$ holds. The cross-product $\mathsf{z} \times \mathsf{R}$ is defined as mapping $(\mathsf{z} \times \mathsf{R}) : \mathbb{R}^3 \to \mathbb{R}^3$, $\mathsf{y} \mapsto \mathsf{z} \times (\mathsf{R} \cdot \mathsf{y})$. Moreover, canonical basis vectors in $\mathbb{R}^3$ are denoted by e_i, $i = 1, 2, 3$, for example, $\mathsf{e}_1 = (1, 0, 0)$. Then, the stationary Cosserat rod model stated in the director basis for a spun glass jet reads

$$
\begin{aligned}
\partial_s \check{\mathsf{r}} &= \mathsf{R}^{\mathrm{T}} \cdot \mathsf{e}_3, \\
\partial_s \mathsf{R} &= -\kappa \times \mathsf{R}, \\
\partial_s \kappa &= -\frac{\rho}{3Q}\frac{\kappa n_3}{\mu} + \frac{4\pi\rho^2}{3Q^2}\frac{u}{\mu}\mathsf{P}_{3/2} \cdot \mathsf{m}, \\
\partial_s u &= \frac{\rho}{3Q}\frac{u n_3}{\mu}, \\
\partial_s \mathsf{n} &= -\kappa \times \mathsf{n} + Qu\kappa \times \mathsf{e}_3 + \frac{\rho}{3}\frac{u n_3}{\mu}\mathsf{e}_3 + 2Q\Omega(\mathsf{R} \cdot \mathsf{e}_1) \times \mathsf{e}_3 \\
&\quad + Q\Omega^2\frac{1}{u}\mathsf{R} \cdot \left(\mathsf{e}_1 \times (\mathsf{e}_1 \times \check{\mathsf{r}})\right) + Qg\frac{1}{u}\mathsf{R} \cdot \mathsf{e}_1 - \mathsf{R} \cdot \check{\mathsf{f}}_{air}, \\
\partial_s \mathsf{m} &= -\kappa \times \mathsf{m} + \mathsf{n} \times \mathsf{e}_3 + \frac{\rho}{3}\frac{u}{\mu}\mathsf{P}_3 \cdot \mathsf{m} - \frac{Q}{12\pi}\frac{n_3}{\mu}\mathsf{P}_2 \cdot \kappa \\
&\quad - \frac{Q\Omega}{12\pi}\frac{n_3}{\mu u}\mathsf{P}_2 \cdot (\mathsf{R} \cdot \mathsf{e}_1) - \frac{Q^2\Omega}{4\pi\rho}\frac{1}{u}\mathsf{P}_2 \cdot (\kappa \times \mathsf{R} \cdot \mathsf{e}_1) \\
&\quad - \frac{Q^2}{4\pi\rho}\frac{1}{u^2}\mathsf{P}_2 \cdot (u\kappa + \Omega\mathsf{R} \cdot \mathsf{e}_1) \times (u\kappa + \Omega\mathsf{R} \cdot \mathsf{e}_1), \\
\partial_s T &= \frac{1}{c_p Q}(q_{rad} + q_{air})
\end{aligned}
\tag{5}
$$

with $q_{rad} = 2\sqrt{\pi}\varepsilon_R\sigma\sqrt{Q/\rho}(T_{ref}^4 - T^4)/\sqrt{u}$ and diagonal matrix $\mathsf{P}_k = \mathrm{diag}(1, 1, k)$, $k \in \mathbb{R}$. For a spun jet emerging from the centrifugal disk at $s = 0$ with stress-free end at $s = L$, the equations are supplemented with

$$
\begin{aligned}
&\check{\mathsf{r}}(0) = (H, R, 0), \quad \mathsf{R}(0) = \mathsf{e}_1 \otimes \mathsf{e}_1 - \mathsf{e}_2 \otimes \mathsf{e}_3 + \mathsf{e}_3 \otimes \mathsf{e}_2, \\
&\kappa(0) = \mathsf{0}, \quad u(0) = U, \quad T(0) = \theta, \\
&\mathsf{n}(L) = \mathsf{0}, \quad \mathsf{m}(L) = \mathsf{0}
\end{aligned}
$$

(cf. Table 1). Considering the jet as representative of one spinning row, we choose the nozzle position to be $(H, R, 0)$ with respective height H, R is here the disk radius. The initialization $\mathsf{R}(0)$ prescribes the jet direction at the nozzle as $(\mathbf{d_1}, \mathbf{d_2}, \mathbf{d_3})(0) = (\mathbf{a_1}, -\mathbf{a_3}, \mathbf{a_2})$.

Remark 1 *The rotations* $\mathsf{R} \in \mathrm{SO}(3)$ *can be parameterized, for example, in Euler angles or unit quaternions* [39]. *The last variant offers a very elegant way of rewriting*

the second equation of (5). *Define*

$$\mathsf{R}(\mathsf{q}) = \begin{pmatrix} q_1^2 - q_2^2 - q_3^2 + q_0^2 & 2(q_1q_2 - q_0q_3) & 2(q_1q_3 + q_0q_2) \\ 2(q_1q_2 + q_0q_3) & -q_1^2 + q_2^2 - q_3^2 + q_0^2 & 2(q_2q_3 - q_0q_1) \\ 2(q_1q_3 - q_0q_2) & 2(q_2q_3 + q_0q_1) & -q_1^2 - q_2^2 + q_3^2 + q_0^2 \end{pmatrix},$$

$\mathsf{q} = (q_0, q_1, q_2, q_3)$ *with* $\|\mathsf{q}\| = 1$, *then we have* $\partial_s \mathsf{q} = \mathcal{A}(\kappa) \cdot \mathsf{q}$ *with skew-symmetric matrix*

$$\mathcal{A}(\kappa) = \frac{1}{2} \begin{pmatrix} 0 & \kappa_1 & \kappa_2 & \kappa_3 \\ -\kappa_1 & 0 & \kappa_3 & -\kappa_2 \\ -\kappa_2 & -\kappa_3 & 0 & \kappa_1 \\ -\kappa_3 & \kappa_2 & -\kappa_1 & 0 \end{pmatrix}.$$

3.1.2 Rotationally invariant air flow

Due to the spinning set-up the jets emerging from the rotating device form row-wise dense curtains. As a consequence of a row-wise homogenization, the air flow (2) can be treated as stationary not only in the rotating outer basis $\{\mathbf{a_1}(t), \mathbf{a_2}(t), \mathbf{a_3}(t)\}$, but also in a fixed outer one. Because of the symmetry with respect to the rotation axis, it is convenient to introduce cylindrical coordinates $(x, r, \phi) \in \mathbb{R} \times \mathbb{R}^+ \times [0, 2\pi)$ for the space and to attach a cylindrical basis $\{\mathbf{e_x}, \mathbf{e_r}, \mathbf{e_\phi}\}$ with $\mathbf{e_x} = \mathbf{a_1}$ to each space point. The components to an arbitrary vector field $\mathbf{z} \in \mathbb{E}^3$ are indicated by $\hat{\mathsf{z}} = (z_x, z_r, z_\phi) \in \mathbb{R}^3$. Then, taking advantage of the rotational invariance, the stationary Navier-Stokes equations in (x, r) simplify to

$$\begin{aligned}
&\partial_x(\rho_\star v_{x\star}) + \frac{1}{r}\partial_r(r\rho_\star v_{r\star}) = 0, \\
&\partial_x(\rho_\star v_{x\star}^2) + \frac{1}{r}\partial_r(r\rho_\star v_{r\star} v_{x\star}) \\
&\quad = -\partial_x p_\star + \partial_x(2\mu_\star \partial_x v_{x\star} + \lambda_\star \nabla \cdot \hat{\mathsf{v}}_\star) \\
&\qquad + \frac{1}{r}\partial_r\big(r\mu_\star(\partial_x v_{r\star} + \partial_r v_{x\star})\big) - \rho_\star g + (f_x)_{jets}, \\
&\partial_x(\rho_\star v_{x\star} v_{r\star}) + \frac{1}{r}\partial_r(r\rho_\star v_{r\star}^2) - \frac{1}{r}\rho_\star v_{\phi\star}^2 \\
&\quad = -\partial_r p_\star + \partial_x\big(\mu_\star(\partial_x v_{r\star} + \partial_r v_{x\star})\big) \\
&\qquad + \frac{2}{r}\partial_r(r\mu_\star \partial_r v_{r\star}) + \partial_r(\lambda_\star \nabla \cdot \hat{\mathsf{v}}_\star) - \frac{2}{r^2}\mu_\star v_{r\star} + (f_r)_{jets}, \\
&\partial_x(\rho_\star v_{x\star} v_{\phi\star}) + \frac{1}{r}\partial_r(r\rho_\star v_{r\star} v_{\phi\star}) + \frac{1}{r}\rho_\star v_{r\star} v_{\phi\star} \\
&\quad = \partial_x(\mu_\star \partial_x v_{\phi\star}) + \frac{1}{r^2}\partial_r\left(r^3 \mu_\star \partial_r\left(\frac{1}{r} v_{\phi\star}\right)\right) + (f_\phi)_{jets},
\end{aligned} \tag{6}$$

$$
\begin{aligned}
&\partial_x(\rho_\star e_\star v_{x\star}) + \frac{1}{r}\partial_r(r\rho_\star e_\star v_{r\star}) \\
&\quad = \mu_\star\Big[2(\partial_x v_{x\star})^2 + 2(\partial_r v_{r\star})^2 + (\partial_x v_{r\star} + \partial_r v_{x\star})^2 \\
&\qquad + (\partial_x v_{\phi\star})^2 + \left(r\partial_r\left(\frac{1}{r}v_{r\star}\right)\right)^2 + \frac{2}{r^2}v_{r\star}^2\Big] \\
&\qquad + \lambda_\star(\nabla\cdot\hat{\mathsf{v}}_\star)^2 - p_\star\nabla\cdot\hat{\mathsf{v}}_\star + \partial_x(k_\star\partial_x T_\star) + \frac{1}{r}\partial_r(rk_\star\partial_r T_\star) + q_{jets}
\end{aligned}
$$

with $\nabla\cdot\hat{\mathsf{v}}_\star = \partial_x v_{x\star} + (\partial_r(r v_{r\star}))/r$ and equipped with appropriate inflow, outflow and wall boundary conditions, cf. Figures 1 and 2.

3.2 Exchange functions

To perform the coupling between (5) and (6), we have to compute the exchange functions in the appropriate coordinates. These calculations are simplified by the rotational invariance of the problem. As introduced, we use the subscripts $\check{}$ and $\hat{}$ to indicate the component tuples corresponding to the rotating outer basis $\{\mathbf{a_1}(t), \mathbf{a_2}(t), \mathbf{a_3}(t)\}$ and the cylindrical basis $\{\mathbf{e_x}, \mathbf{e_r}, \mathbf{e_\phi}\}$, respectively. Essentially for the coupling are the jet tangent and the relative velocity between air flow and glass jet, they are

$$
\begin{aligned}
\check{\tau} &= \mathsf{R}^{\mathrm{T}}\cdot\mathsf{e}_3, \\
\hat{\tau} &= \left(\check{\tau}_1, \frac{\check{r}_2\check{\tau}_2 + \check{r}_3\check{\tau}_3}{\sqrt{\check{r}_2^2+\check{r}_3^2}}, \frac{\check{r}_2\check{\tau}_3 - \check{r}_3\check{\tau}_2}{\sqrt{\check{r}_2^2+\check{r}_3^2}}\right)
\end{aligned}
$$

and

$$
\begin{aligned}
\check{\mathsf{v}}_{rel} &= \left(v_{x\star}, \frac{\check{r}_2 v_{r\star} - \check{r}_3(v_{\phi\star}-\Omega r)}{\sqrt{\check{r}_2^2+\check{r}_3^2}}, \frac{\check{r}_3 v_{r\star} + \check{r}_2(v_{\phi\star}-\Omega r)}{\sqrt{\check{r}_2^2+\check{r}_3^2}}\right) - u\check{\tau}, \\
\hat{\mathsf{v}}_{rel} &= (v_{x\star}, v_{r\star}, v_{\phi\star}-\Omega r) - u\hat{\tau}.
\end{aligned}
$$

Then, the drag forces are

$$
\begin{aligned}
\check{\mathsf{f}}_{air}(s) &= \check{\mathcal{F}}\big(\Psi(s), \Psi_\star\big(\check{r}_1(s), \sqrt{\check{r}_2^2(s)+\check{r}_3^2(s)}\big)\big), \\
\hat{\mathsf{f}}_{jets}(x,r) &= -\frac{N}{2\pi}\int_I \frac{1}{r}\delta\big(x-\check{r}_1(s)\big)\delta\big(r-\sqrt{\check{r}_2^2(s)+\check{r}_3^2(s)}\big)\hat{\mathcal{F}}\big(\Psi(s), \Psi_\star(x,r)\big)\,\mathrm{d}s, \\
\check{\mathcal{F}}(\Psi,\Psi_\star) &= 2\sqrt{\frac{Q}{\pi\rho}}\frac{\mu_\star^2}{\rho_\star}\frac{1}{\sqrt{u}}\mathrm{F}\left(\check{\tau}, 2\sqrt{\frac{Q}{\pi\rho}}\frac{\rho_\star}{\mu_\star}\frac{1}{\sqrt{u}}\check{\mathsf{v}}_{rel}\right), \\
\hat{\mathcal{F}}(\Psi,\Psi_\star) &= 2\sqrt{\frac{Q}{\pi\rho}}\frac{\mu_\star^2}{\rho_\star}\frac{1}{\sqrt{u}}\mathrm{F}\left(\hat{\tau}, 2\sqrt{\frac{Q}{\pi\rho}}\frac{\rho_\star}{\mu_\star}\frac{1}{\sqrt{u}}\hat{\mathsf{v}}_{rel}\right)
\end{aligned}
$$

and the heat sources

$$q_{air}(s) = \mathcal{Q}\big(\Psi(s), \Psi_\star\big(\check{r}_1(s), \sqrt{\check{r}_2^2(s) + \check{r}_3^2(s)}\big)\big),$$

$$q_{jets}(x,r) = -\frac{N}{2\pi}\int_I \frac{1}{r}\delta\big(x - \check{r}_1(s)\big)\delta\big(r - \sqrt{\check{r}_2^2(s) + \check{r}_3^2(s)}\big)\mathcal{Q}\big(\Psi(s), \Psi_\star(x,r)\big)\,\mathrm{d}s,$$

$$\mathcal{Q}(\Psi, \Psi_\star) = 2k_\star(T_\star - T)\mathrm{Nu}\left(\frac{\check{\mathrm{v}}_{rel}}{\|\check{\mathrm{v}}_{rel}\|}\cdot\check{\tau}, \sqrt{\frac{\pi Q}{\rho}}\frac{\rho_\star}{\mu_\star}\frac{\|\check{\mathrm{v}}_{rel}\|}{\sqrt{u}}, \frac{\mu_\star c_{p\star}}{k_\star}\right).$$

Here, $\hat{\mathrm{f}}_{jets}$ and q_{jets} represent the homogenized effect of the N glass jets emerging from the equidistantly placed holes in an arbitrary spinning row. Correspondingly, system (5) with $\check{\mathrm{f}}_{air}$ and q_{air} describes one representative glass jet for this row. To simulate the full problem with all MN glass jets in the air, jet representatives Ψ_i, $i = 1, \ldots, M$ for all M spinning rows with the respective boundary and air flow conditions have to be determined. Their common effect on the air flow is

$$\hat{\mathrm{f}}_{jets}(x,r) = -\frac{N}{2\pi}\sum_{i=1}^{M}\int_{I_i}\frac{1}{r}\delta\big(x - \check{r}_{1,i}(s)\big)\delta\big(r - \sqrt{\check{r}_{2,i}^2(s) + \check{r}_{3,i}^2(s)}\big)\hat{\mathcal{F}}\big(\Psi_i(s), \Psi_\star(x,r)\big)\,\mathrm{d}s,$$

$$q_{jets}(x,r) = -\frac{N}{2\pi}\sum_{i=1}^{M}\int_{I_i}\frac{1}{r}\delta\big(x - \check{r}_{1,i}(s)\big)\delta\big(r - \sqrt{\check{r}_{2,i}^2(s) + \check{r}_{3,i}^2(s)}\big)\mathcal{Q}\big(\Psi_i(s), \Psi_\star(x,r)\big)\,\mathrm{d}s.$$

4 Numerical treatment

The numerical simulation of the glass jets dynamic in the air flow is performed by an algorithm that weakly couples glass jet calculation and air flow computation *via* iterations. This procedure is adequate for the problem and has the advantage that we can combine commercial software and self-implemented code. We use FLUENT, a commercial finite volume-based software by ANSYS, that contains the broad physical modeling capabilities needed to describe air flow, turbulence and heat transfer for the industrial glass wool manufacturing process. In particular, a pressure-based solver is applied in the computation of (6). To restrict the computational effort in grid refinement needed for the resolution of the turbulent air streams we consider alternatively a stochastic k-ω turbulence model. (For details on the commercial software FLUENT, its models and solvers we refer to http://www.fluent.com.) Note that the modification of the model equations has no effect on our coupling framework, where the exchange functions are incorporated by UDFs (user defined functions). For the boundary value problem of the stationary Cosserat rod (5), systems of nonlinear equations are set up *via* a Runge-Kutta collocation method and solved by a Newton method in MATLAB 7.4. The convergence of the Newton method depends thereby crucially on the initial guess. To improve the computational performance we adapt the initial guess

iteratively by solving a sequence of boundary value problems with slightly changed parameters. The developed continuation method is presented in the following. Moreover, to get a balanced numerics we use the dimensionless rod system that is scaled with the respective conditions at the nozzle. The M glass jet representative are computed in parallel. The exchange of flow and fiber data between the solvers is based on interpolation and averaging, as we explain in the weak iterative coupling algorithm.

4.1 Collocation-continuation method for dimensionless rod boundary value problem

The computing of the glass jets is based on a dimensionless rod system. For this purpose, we scale the dimensional equations (5) with the spinning conditions of the respective row. Apart from the air flow data, (5) contains thirteen physical parameters, that is, jet density ρ, heat capacity c_p, emissivity ε_R, typical length L, velocity U and temperature θ at the spinning hole as well as hole diameter D and height H, centrifugal disk radius R, rotational frequency Ω, reference temperature for radiation T_{ref} and gravitational acceleration g. The typical jet viscosity is chosen to be $\mu_0 = \mu(\theta)$. These induce various dimensionless numbers characterizing the fiber spinning, that is, Reynolds number Re as ratio between inertia and viscosity, Rossby number Rb as ratio between inertia and rotation, Froude number Fr as ratio between inertia and gravity and Ra as ratio between radiation and heat advection as well as ℓ, h and ϵ as length ratios between jet length, hole height, diameter and disk radius, respectively,

$$\mathrm{Re} = \frac{\rho U R}{\mu_0}, \quad \mathrm{Rb} = \frac{U}{\Omega R}, \quad \mathrm{Fr} = \frac{U}{\sqrt{gR}}, \quad \mathrm{Ra} = \frac{4\varepsilon_R \sigma \theta^3 R}{\rho c_p U D},$$
$$\ell = \frac{L}{R}, \quad h = \frac{H}{R}, \quad \epsilon = \frac{D}{R}.$$

In addition, we introduce dimensionless quantities that also depend on local air flow data, similarly to the Nusselt number in (4)

$$\mathrm{A}_1 = \frac{4\mu_\star^2 R}{\pi \rho_\star \rho U^2 D^3}, \quad \mathrm{A}_2 = \frac{\rho_\star U D}{\mu_\star}, \quad \mathrm{A}_3 = \frac{8 k_\star R}{\pi \rho c_p \theta D^2}, \quad \mathrm{A}_4 = \frac{\mu_\star c_{p\star}}{k_\star}.$$

Here, A_4 is the Prandtl number of the air flow. To make (5) dimensionless we use the following reference values:

$$s_0 = L, \quad r_0 = R, \quad \kappa_0 = R^{-1},$$
$$u_0 = U, \quad T_0 = \theta, \quad \mu_0 = \mu(T_0),$$
$$n_0 = \pi \mu_0 U D^2/(4R), \quad m_0 = \pi \mu_0 U D^4/(16R^2).$$

We choose the disk radius R as macroscopic length scale in the scalings, since it is well known by the set-up. As for L, we consider jet lengths where the stresses are supposed to be vanished. In general, R and L are of same order such that the parameter ϵ can be identified with the slenderness ratio δ of the jets, cf. Introduction. The last two scalings for n_0 and m_0 are motivated by the material laws and the fact that

the mass flux is $Q = \pi\rho U D^2/4$. Then, the dimensionless system for the stationary viscous rod has the form

$$
\begin{aligned}
\frac{1}{\ell}\partial_s \check{\mathsf{r}} &= \mathsf{R}^{\mathrm{T}} \cdot \mathsf{e}_3 = \check{\tau},\\
\frac{1}{\ell}\partial_s \mathsf{R} &= -\kappa \times \mathsf{R},\\
\frac{1}{\ell}\partial_s \kappa &= -\frac{1}{3\mu}\kappa n_3 + \frac{4}{3\mu} u \mathsf{P}_{3/2} \cdot \mathsf{m},\\
\frac{1}{\ell}\partial_s u &= \frac{1}{3\mu} u n_3,\\
\frac{1}{\ell}\partial_s \mathsf{n} &= -\kappa \times \mathsf{n} + \mathrm{Re} u \left(\kappa \times \mathsf{e}_3 + \frac{1}{3\mu} n_3 \mathsf{e}_3 \right)\\
&\quad + \frac{2\mathrm{Re}}{\mathrm{Rb}} (\mathsf{R} \cdot \mathsf{e}_1) \times \mathsf{e}_3 + \frac{\mathrm{Re}}{\mathrm{Rb}^2} \frac{1}{u} \mathsf{R} \cdot \left(\mathsf{e}_1 \times (\mathsf{e}_1 \times \check{\mathsf{r}}) \right)\\
&\quad + \frac{\mathrm{Re}}{\mathrm{Fr}^2} \frac{1}{u} \mathsf{R} \cdot \mathsf{e}_1 - \mathrm{Re} \mathrm{A}_1 \sqrt{u} \mathsf{R} \cdot \mathrm{F}\left(\check{\tau}, \mathrm{A}_2 \frac{1}{\sqrt{u}} \check{\mathsf{v}}_{rel} \right),\\
\frac{1}{\ell}\partial_s \mathsf{m} &= -\kappa \times \mathsf{m} + \frac{4}{\epsilon^2} \mathsf{n} \times \mathsf{e}_3 + \frac{\mathrm{Re}}{3\mu} \left(u \mathsf{P}_3 \cdot \mathsf{m} - \frac{1}{4} n_3 \mathsf{P}_2 \cdot \kappa \right)\\
&\quad - \frac{\mathrm{Re}}{4\mathrm{Rb}} \frac{1}{u} \mathsf{P}_2 \cdot \left(\frac{1}{3\mu} \mathsf{R} \cdot \mathsf{e}_1 n_3 + \kappa \times \mathsf{R} \cdot \mathsf{e}_1 \right)\\
&\quad - \frac{\mathrm{Re}}{4} \left(\frac{1}{u^2} \mathsf{P}_2 \cdot \left(u\kappa + \frac{1}{\mathrm{Rb}} \mathsf{R} \cdot \mathsf{e}_1 \right) \right) \times \left(u\kappa + \frac{1}{\mathrm{Rb}} \mathsf{R} \cdot \mathsf{e}_1 \right),\\
\frac{1}{\ell}\partial_s T &= \mathrm{Ra} \frac{1}{\sqrt{u}} \left(T_{ref}^4 - T^4 \right)\\
&\quad + \mathrm{A}_3 (T_\star - T) \mathrm{Nu} \left(\frac{\check{\mathsf{v}}_{rel}}{\|\check{\mathsf{v}}_{rel}\|} \cdot \check{\tau}, \frac{\pi \mathrm{A}_2}{2} \frac{\|\check{\mathsf{v}}_{rel}\|}{\sqrt{u}}, \mathrm{A}_4 \right),
\end{aligned}
\tag{7}
$$

with

$$
\begin{aligned}
&\check{\mathsf{r}}(0) = (h, 1, 0), \quad \mathsf{R}(0) = \mathsf{e}_1 \otimes \mathsf{e}_1 - \mathsf{e}_2 \otimes \mathsf{e}_3 + \mathsf{e}_3 \otimes \mathsf{e}_2,\\
&\kappa(0) = 0, \quad u(0) = 1, \quad T(0) = 1,\\
&\mathsf{n}(1) = 0, \quad \mathsf{m}(1) = 0.
\end{aligned}
$$

Here, T_{ref} and the air flow associated $T_\star$ and $\check{\mathsf{v}}_{rel}$ are scaled with θ and U, respectively. System (7) contains the slenderness parameter ϵ ($\epsilon \ll 1$) explicity in the equation for the couple m and is hence no asymptotic model of zeroth order. In the slenderness limit $\epsilon \to 0$, the rod model reduces to a string system and their solutions for $(\check{\mathsf{r}}, \check{\tau}, u, N = n_3, T)$ coincide. Only these jet quantities are relevant for the two-way coupling, as they enter in the exchange functions. However, the simpler string system is not well-posed for all parameter ranges, [15, 16]. Thus, it makes sense to consider

(7) as ϵ-regularized string system, [19]. We treat ϵ as moderate fixed regularization parameter in the following to stabilize the numerics, in particular we set $\epsilon = 0.1$.

For the numerical treatment of (7), systems of non-linear equations are set up *via* a Runge-Kutta collocation method and solved by a Newton method. The Runge-Kutta collocation method is an integration scheme of fourth order for boundary value problems, that is, $\partial_s \mathsf{z} = \mathsf{f}(s, \mathsf{z})$, $\mathsf{f} : [a, b] \times \mathbb{R}^n \to \mathbb{R}^n$ with $\mathsf{g}(\mathsf{z}(a), \mathsf{z}(b)) = 0$. It is a standard routine in MATLAB 7.4 with adaptive grid refinement (solver `bvp4c.m`). Let $a = s_0 < s_1 < \cdots < s_N = b$ be the collocation points in $[a, b]$ with $h_i = s_i - s_{i-1}$ and denote $\mathsf{z}_\mathsf{i} = \mathsf{z}(s_i)$. Then, the nonlinear system of $(N + 1)$ equations, $\mathsf{S}(\mathsf{z}^h) = 0$, for the discrete solution $\mathsf{z}^h = (\mathsf{z}_\mathsf{i})_{i=0,\ldots,N}$ is set up *via*

$$\mathsf{S}_0\big(\mathsf{z}^h\big) = \mathsf{g}(\mathsf{z}_0, \mathsf{z}_\mathsf{N}) = 0,$$

$$\mathsf{S}_{\mathsf{i}+1}\big(\mathsf{z}^h\big) = \mathsf{z}_{\mathsf{i}+1} - \mathsf{z}_\mathsf{i} - \frac{h_{i+1}}{6}\big(\mathsf{f}(s_i, \mathsf{z}_\mathsf{i}) + 4\mathsf{f}(s_{i+1/2}, \mathsf{z}_{\mathsf{i}+1/2}) + \mathsf{f}(s_{i+1}, \mathsf{z}_{\mathsf{i}+1})\big) = 0,$$

$$\mathsf{z}_{\mathsf{i}+1/2} = \frac{1}{2}(\mathsf{z}_{\mathsf{i}+1} + \mathsf{z}_\mathsf{i}) - \frac{h_{i+1}}{8}\big(\mathsf{f}(s_{i+1}, \mathsf{z}_{\mathsf{i}+1}) - \mathsf{f}(s_i, \mathsf{z}_\mathsf{i})\big)$$

for $i = 0, \ldots, N - 1$. The convergence and hence the computational performance of the Newton method depends crucially on the initial guess. Thus, we adapt the initial guess iteratively by help of a continuation strategy. We scale the drag function F with the factor $\mathrm{C_F^{-2}}$ and the right-hand side of the temperature equation with C_T and treat Re, Rb, Fr, ℓ, $\mathrm{C_F}$ and C_T as continuation parameters. We start from the solution for $(\mathrm{Re}, \mathrm{Rb}, \mathrm{Fr}, \ell, \mathrm{C_F}, \mathrm{C}_T) = (1, 1, 1, 0.15, \infty, 0)$ which corresponds to an isothermal rod without aerodynamic forces that has been intensively numerically investigated in [19]. Its determination is straight forward using the related string model as initial guess. Note that we choose ℓ so small to ensure that the glass jet lies in the air flow domain. The actual continuation is then divided into three parts. First, $(\mathrm{Re}, \mathrm{Rb}, \mathrm{Fr}, \mathrm{C_F})$ are adjusted, then C_T and finally ℓ. In the continuation we use an adaptive step size control. Thereby, we always compute the interim solutions by help of one step and two half steps and decide with regard to certain quality criteria whether the step size should be increased or decreased.

4.2 Weak iterative coupling algorithm

The numerical difficulty of the coupling of glass jet and air flow computations, $\mathcal{S}_{jets}$ and $\mathcal{S}_{air}$, results from the different underlying discretizations. Let I_h denote the rod grid used in the continuation method and I_Δ be an equidistant grid of step size Δs with respective jet data Ψ_Δ for data exchange. Moreover, let Ω_h denote the finite volume mesh with the flow data $\Psi_{\star,V}$ for the cell V, (so the chosen mesh realizes the necessary averaging). For the air associated exchange functions, the flow data is linearly interpolated on I_h. Precisely, the linear interpolation $\mathbb{L}$ with respect to $\check{\mathsf{r}}(s_j)$, $s_j \in I_h$ is performed over all $V \in \mathcal{N}(s_j)$, where $\mathcal{N}(s_j)$ is the set of the cell containing $\check{\mathsf{r}}(s_j)$ and its direct neighbor cells,

$$\check{\mathsf{f}}_{air}(s_j) \approx \check{\mathcal{F}}\big(\Psi(s_j), \mathbb{L}_{\mathcal{N}(s_j)}[\Psi_{\star,V}]\big),$$

$$q_{air}(s_j) \approx \mathcal{Q}\big(\Psi(s_j), \mathbb{L}_{\mathcal{N}(s_j)}[\Psi_{\star,V}]\big).$$

For the jet associated exchange functions entering the finite volume scheme, we need the averaged jet information for every cell $V \in \Omega_h$. We introduce $I_{\Delta,V} = \{s_j \in I_\Delta | \check{\mathrm{r}}(s_j) \in V\}$ and $|I_V| = \Delta s |I_{\Delta,V}|$, then the averaging $\mathbb{E}$ with respect to V is performed over the $I_{\Delta,V}$-associated data,

$$\frac{2\pi}{|V|}\int_V r\hat{\mathrm{f}}_{jets}(x,r)\,\mathrm{d}x\,\mathrm{d}r \approx -\frac{N|I_V|}{|V|}\hat{\mathcal{F}}\big(\mathbb{E}_V[\Psi_\Delta], \Psi_{\star,V}\big),$$
$$\frac{2\pi}{|V|}\int_V r q_{jets}(x,r)\,\mathrm{d}x\,\mathrm{d}r \approx -\frac{N|I_V|}{|V|}\mathcal{Q}\big(\mathbb{E}_V[\Psi_\Delta], \Psi_{\star,V}\big).$$

The ratio $|I_V|/|V|$ can be considered as the jet length density for the cell V. In case of M jet representatives, we deal with $I_{\Delta,V,i}$ and $|I_{V,i}|$ for $i = 1,\ldots,M$. Consequently, we have $I_{\Delta,V} = \bigcup_{i=1}^M I_{\Delta,V,i}$ and $|I_V| = \sum_{i=1}^M |I_{V,i}|$. Note, that the interpolation and averaging approximation strategies have the disadvantage that they are qualitatively different. Thus, momentum and energy conservation are only ensured for very fine resolutions.

Summing up, the algorithm that we use to couple glass jet $\mathcal{S}_{jets}$ and air flow $\mathcal{S}_{air}$ computations has the form:

Algorithm 1
Generate flow mesh Ω_h
Perform flow simulation $\mathcal{S}_{air}$ *without jets to obtain* $\Psi_\star^{(0)}$
Initialize $k = 0$
Do

- *Compute*: $\Psi_i^{(k)} = \mathcal{S}_{jets}(\Psi_\star^{(k)})$ *for* $i = 1,\ldots,M$ *where flow data is linearly interpolated on* I_h
- *Interpolate jet data on equidistant grid* I_Δ
- *Find for every cell* V *in* Ω_h *the relevant rod points* $I_{\Delta,V}$ *and average the respective data*
- *Compute*: $\Psi_\star^{(k+1)} = \mathcal{S}_{air}(\Psi^{(k)})$
- *Update*: $k = k+1$

while $\|\Psi^{(k)} - \Psi^{(k-1)}\| > tol$

Remark 2 *From the technical point of view, the efficient management of the simulation and coupling routines is quite demanding. In a preprocessing step we generate the finite volume mesh* Ω_h *via the software Gambit and save it in a file that is available for FLUENT and MATLAB. The program of Algorithm 1 is then realized with FLUENT as master tool. After the air flow simulation FLUENT starts MATLAB. MATLAB governs the parallelization of the jets computation via MATLAB executables. Collecting the jets information, it provides the averaged jets data on* Ω_h *in a file. FLUENT reads in this data and performs a new air flow simulation with immersed jets.*

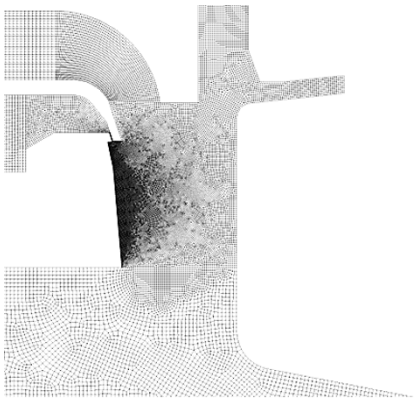

Fig. 4 Finite volume mesh Ω_h for air flow computations (mesh detail).

5 Results

In this section we illustrate the applicability of our asymptotic coupling framework to the given rotational spinning process. We show the convergence of the weak iterative coupling algorithm and discuss the effects of the fluid-fiber-interactions.

For all air flow simulations we use the same finite volume mesh Ω_h whose refinement levels are initially chosen according to the unperturbed flow structure, independently of the glass jets. This implies a very fine resolution at the injector of the turbulent cross flow which is coarsen towards the centrifugal disk. For mesh details see Figure 4. The turbulent intensity is visualized in Figure 5. As expected it is high at the injector and moderate in the remaining flow domain. In particular, it is less than 2% in the region near the centrifugal disk where the glass jets will be presumably located. Thus, we neglect turbulence effects on the jets dynamics in the following. However, note that such effects can be easily incorporated by help of stochastic drag models [24, 37, 40] that are based on RANS turbulence descriptions (for example, k-ϵ model or k-ω model). For the jet computations the grid I_h is automatically generated and adapted by the continuation method in every iteration. To ensure that sufficient jet points lie in each flow cell and a proper data exchange is given we use an equidis-

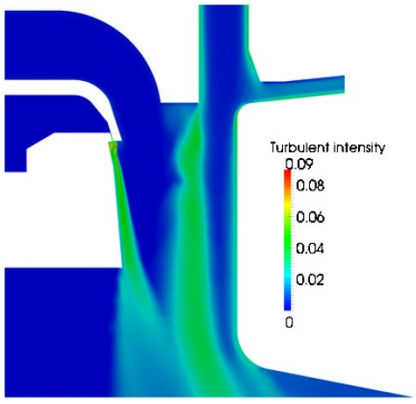

Fig. 5 Turbulent intensity of the air flow.

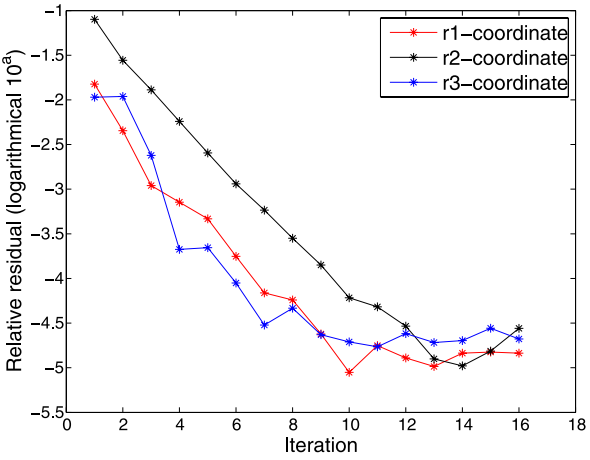

Fig. 6 Convergence of the weak iterative coupling algorithm. Relative error of all M curve coordinates in $\mathcal{L}^2(I)$-norm over number of iterations, plotted in logarithmic scale.

tant grid I_Δ with appropriate step size Δs (at minimum 2 jet points per interacting flow cell).

The weak iterative coupling algorithm is fully automated. Each iteration starts with the same initialization. There is no parameter adjustment. The algorithm turns out to be very robust and reliable in spite of coarse flow meshes. For our set-up an air flow simulation takes around 30 minutes CPU-time, and the computation of a single jet takes approximatively just as long. The algorithm converges within 12-14 iterations. Figure 6 shows the relative $\mathcal{L}^2$-error of all jet curve components over the number of iterations k, that is,

$$\sum_{i=1}^{M} \frac{\|\breve{r}_{j,i}^{(k)} - \breve{r}_{j,i}^{f}\|_{\mathcal{L}^2(I_i)}}{\|\breve{r}_{j,i}^{f}\|_{\mathcal{L}^2(I_i)}}, \quad \text{with } \breve{r}_{j,i}^{f} \text{ final solution, } j = 1, 2, 3.$$

The effects of the fluid-fiber interactions and the necessity of the two-way coupling procedure for the rotational spinning process can be concluded from the following results. Figure 7 shows the swirl velocity of the air flow and the location of the im-

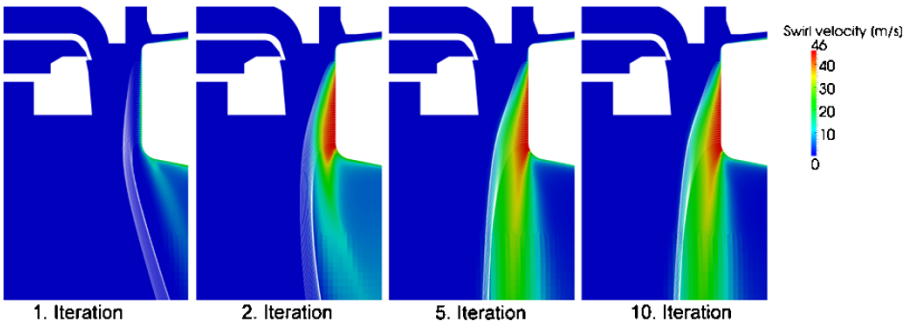

Fig. 7 Illustration of iterative coupling procedure. Iteration results for air swirl velocity and immersed glass jets (plotted as white curves).

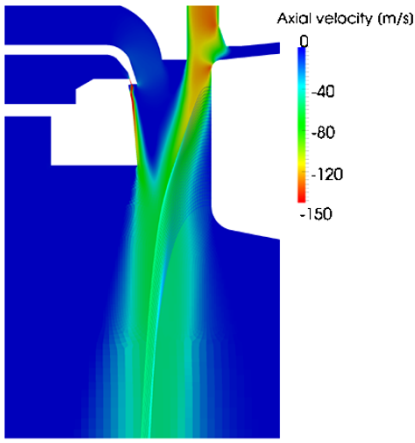

Fig. 8 Final simulation result. Glass jets and air flow in given rotational spinning process. The color map visualizes the axial velocity of the air flow. In addition, the immersed $M = 35$ glass jet representatives are colored with respect to their corresponding quantity u. For temperature information see Figure 9. Moreover, the dynamics and properties of the highest and lowest jets are shown in detail in Figures 10, 11, 12 and 13.

mersed glass jets over the iterations. In the unperturbed flow without the glass jets there is no swirl velocity. In fact, the presence of the jets cause the swirl velocity, since the jets pull the flow with them. Moreover, the jets deflect the downwards directed burner flow, as seen in Figures 8 and 9. The jets behavior looks very reasonable. Trajectories and positions are as expected. Furthermore, their properties, that is, velocity u and temperature T, correspond to the axial flow velocity and flow temperature, which implies a proper momentum and heat exchange. For jet details we refer to Figures 10, 11, 12 and 13. They show the influence of the spinning rows. The jet representative of the highest spinning row is warmer than the one of the lowest row which implies better stretching capabilities. It is also faster and hence thinner ($A = u^{-1}$). This certainly comes from the fact that the highest jet is longer affected by the fast hot burner flow. However, in view of quality assessment, slenderness and homogeneity of the spun fiber jets play an important role. This requires the optimal design of the spinning conditions, for example, different nozzle diameters or various

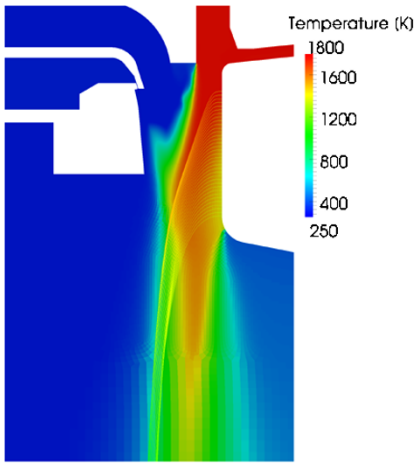

Fig. 9 Final simulation result. Glass jets and air flow in given rotational spinning process. The color maps visualize axial velocity and temperature of the air flow, respectively. In addition, the immersed $M = 35$ glass jet representatives are colored with respect to their corresponding quantity T. For velocity information see Figure 8. Moreover, the dynamics and properties of the highest and lowest jets are shown in detail in Figures 10, 11, 12 and 13.

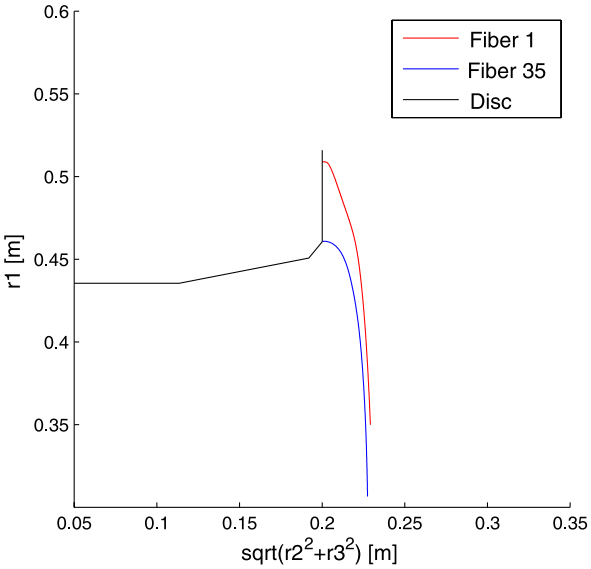

Fig. 10 Dynamics of the jets emerging from the highest and lowest spinning rows of the centrifugal disk. Side view of the plant. See associated Figures 11, 12 and 13.

distances between spinning rows. But for this purpose, also the melting regime has to be taken into account in modeling and simulation which is left to future research.

6 Conclusion

The optimal design of rotational spinning processes for glass wool manufacturing involves the simulation of ten thousands of slender viscous thermal glass jets in fast air

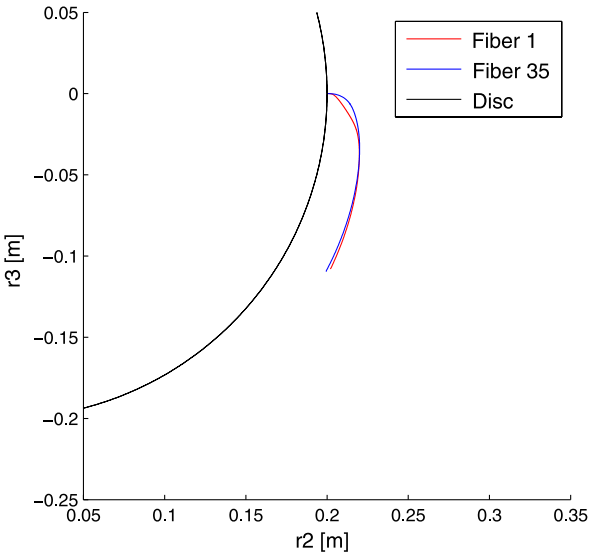

Fig. 11 Dynamics of the jets emerging from the highest and lowest spinning rows of the centrifugal disk. Top view of the plant. See associated Figures 10, 12 and 13.

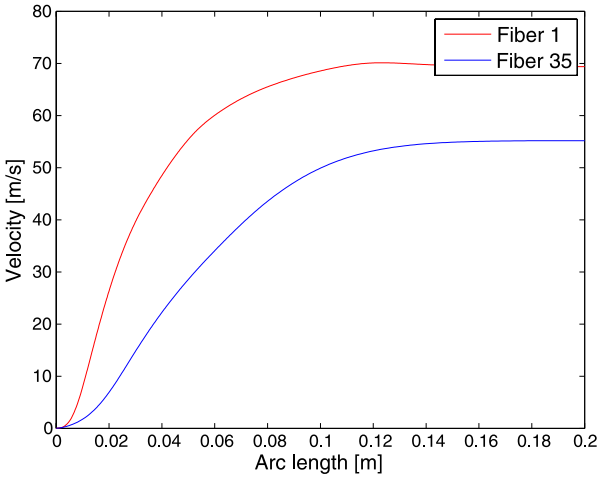

Fig. 12 Dynamics of the jets emerging from the highest and lowest spinning rows of the centrifugal disk. Jets velocity $u(s)$, $s \in [0, L]$. See associated Figures 10, 11 and 13.

streams. This is a computational challenge where direct numerical methods fail. In this paper we have established an asymptotic modeling concept for the fluid-fiber interactions. Based on slender-body theory and homogenization it reduces the complexity of the problem enormously and makes numerical simulations possible. Adequate to problem and model we have proposed an algorithm that weakly couples air flow and glass jets computations *via* iterations. It turns out to be very robust and converges to reasonable results within few iterations. Moreover, the possibility of combining commercial software and self-implemented code yields satisfying efficiency off-the-shelf. The performance might certainly be improved even more by help of future studies. Summing up, our developed asymptotic coupling framework provides a very promising basis for future optimization strategies.

In view of the design of the whole production process the melting regime must be taken into account in modeling and simulation. Melting and spinning regimes influence each other. On one hand the conditions at the spinning rows are crucially

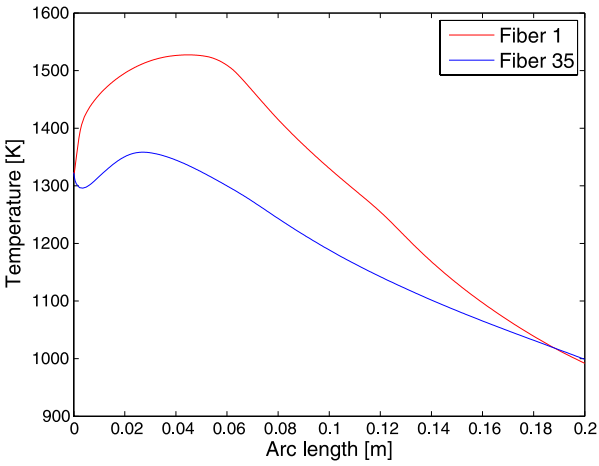

Fig. 13 Dynamics of the jets emerging from the highest and lowest spinning rows of the centrifugal disk. Temperature $T(s)$, $s \in [0, L]$. See associated Figures 10, 11 and 12.

affected by the melt distribution in the centrifugal disk and the burner air flow, regarding, for example, cooling by mixing inside, aerodynamic heating outside. On the other hand the burner flow and the arising heat distortion of the disk are affected by the spun jet curtains. This obviously demands a further coupling procedure.

Competing interests

The authors declare that they have no competing interests.

Authors' contributions

The success of this study is due to the strong and fruitful collaboration of all authors. Even in details it is a joint work. However, special merits go to WA for the numerical analysis of Cosserat rods; to NM for modeling, investigating the asymptotic coupling concept and drafting the manuscript; to JS for conceptualizing and implementing the weak coupling software, performing the simulations and designing the visualizations; and to RW for developing the model framework, investigating the asymptotic coupling concept and implementing the continuation method for the jets. All authors read and approved the final manuscript.

Acknowledgements The authors would like to acknowledge their industrial partner, the company Woltz GmbH in Wertheim, for the interesting and challenging problem. This work has been supported by German Bundesministerium für Bildung und Forschung, Schwerpunkt 'Mathematik für Innovationen in Industrie und Dienstleistungen', Projekt 03MS606 and by German Bundesministerium für Wirtschaft und Technologie, Förderprogramm ZIM, Projekt AUROFA 114626.

References

1. Klar, A., Marheineke, N., Wegener, R.: Hierarchy of mathematical models for production processes of technical textiles. Z. Angew. Math. Mech. **89**, 941–961 (2009)
2. Pearson, J.R.A.: Mechanics of Polymer Processing. Elsevier, London (1985)
3. Decent, S.P., King, A.C., Simmons, M.J.H., Parau, E.I., Wallwork, I.M., Gurney, C.J., Uddin, J.: The trajectory and stability of a spiralling liquid jet: Viscous theory. Appl. Math. Model. **33**(12), 4283–4302 (2009)
4. Parau, E.I., Decent, S.P., King, A.C., Simmons, M.J.H., Wong, D.: Nonlinear viscous liquid jets from a rotating orifice. J. Eng. Math. **57**, 159–179 (2006)
5. Marheineke, N., Wegener, R.: Asymptotic model for the dynamics of curved viscous fibers with surface tension. J. Fluid Mech. **622**, 345–369 (2009)
6. Antman, S.S.: Nonlinear Problems of Elasticity. Springer, New York (2006)
7. Entov, V.M., Yarin, A.L.: The dynamics of thin liquid jets in air. J. Fluid Mech. **140**, 91–111 (1984)
8. Yarin, A.L.: Free Liquid Jets and Films: Hydrodynamics and Rheology. Longman, New York (1993)
9. Cummings, L.J., Howell, P.D.: On the evolution of non-axissymetric viscous fibres with surface tension inertia and gravity. J. Fluid Mech. **389**, 361–389 (1999)
10. Dewynne, J.N., Howell, P.D., Wilmott, P.: Slender viscous fibers with inertia and gravity. Q. J. Mech. Appl. Math. **47**, 541–555 (1994)
11. Dewynne, J.N., Ockendon, J.R., Wilmott, P.: A systematic derivation of the leading-order equations for extensional flows in slender geometries. J. Fluid Mech. **244**, 323–338 (1992)
12. Decent, S.P., King, A.C., Wallwork, I.M.: Free jets spun from a prilling tower. J. Eng. Math. **42**, 265–282 (2002)
13. Panda, S., Marheineke, N., Wegener, R.: Systematic derivation of an asymptotic model for the dynamics of curved viscous fibers. Math. Methods Appl. Sci. **31**, 1153–1173 (2008)
14. Wallwork, I.M., Decent, S.P., King, A.C., Schulkes, R.M.S.M.: The trajectory and stability of a spiralling liquid jet. Part 1. Inviscid theory. J. Fluid Mech. **459**, 43–65 (2002)

15. Götz, T., Klar, A., Unterreiter, A., Wegener, R.: Numerical evidence for the non-existence of solutions to the equations describing rotational fiber spinning. Math. Models Methods Appl. Sci. **18**(10), 1829–1844 (2008)
16. Arne, W., Marheineke, N., Meister, A., Wegener, R.: Numerical analysis of Cosserat rod and string models for viscous jets in rotational spinning processes. Math. Models Methods Appl. Sci. **20**(10), 1941–1965 (2010)
17. Hlod, A., Aarts, A.C.T., van de Ven, A.A.F., Peletier, M.A.: Mathematical model of falling of a viscous jet onto a moving surface. Eur. J. Appl. Math. **18**, 659–677 (2007)
18. Hlod, A., Aarts, A.C.T., van de Ven, A.A.F., Peletier, M.A.: Three flow regimes of viscous jet falling onto a moving surface. ArXiv:0811.2574 (2008)
19. Arne, W., Marheineke, N., Wegener, R.: Asymptotic transition of Cosserat rod to string models for curved viscous inertial jets. Math. Mod. Meth. Appl. Sci. **21**(10) (2011, in press)
20. Ribe, N.M.: Coiling of viscous jets. Proc. R. Soc., Math. Phys. Eng. Sci. **2051**, 3223–3239 (2004)
21. Ribe, N.M., Habibi, M., Bonn, D.: Stability of liquid rope coiling. Phys. Fluids **18**, 084102 (2006)
22. Chiu-Webster, S., Lister, J.R.: The fall of a viscous thread onto a moving surface: A 'fluid-mechanical sewing machine'. J. Fluid Mech. **569**, 89–111 (2006)
23. Ribe, N.M., Lister, J.R., Chiu-Webster, S.: Stability of a dragged viscous thread: Onset of 'stitching' in a fluid-mechanical 'sewing machine'. Phys. Fluids **18**, 124105 (2006)
24. Marheineke, N., Wegener, R.: Modeling and application of a stochastic drag for fiber dynamics in turbulent flows. Int. J. Multiph. Flow **37**, 136–148 (2011)
25. Tomotika, S., Aoi, T., Yosinobu, H.: On the forces acting on a circular cylinder set obliquely in a uniform stream at low values of Reynolds number. Proc. R. Soc., Math. Phys. Eng. Sci. **219**(1137), 233–244 (1953)
26. Batchelor, G.K.: Slender-body theory for particles of arbitrary cross-section in Stokes flow. J. Fluid Mech. **44**(3), 419–440 (1970)
27. Cox, R.G.: The motion of long slender bodies in a viscous fluid. Part 1. General theory. J. Fluid Mech. **44**(4), 791–810 (1970)
28. Taylor, G.I.: Analysis of the swimming of long and narrow animals. Proc. R. Soc., Math. Phys. Eng. Sci. **214**, 158–183 (1952)
29. Sumer, B.M., Fredsoe, J.: Hydrodynamics Around Cylindrical Structures. World Scientific Publishing, London (2006)
30. Schlichting, H.: Grenzschicht-Theorie. Verlag G. Braun, Karlsruhe (1982)
31. Schewe, G.: On the force fluctuations acting on a circular cylinder in cross-flow from subcritical up to transcritical Reynolds numbers. J. Fluid Mech. **133**, 265–285 (1983)
32. Tritton, D.J.: Experiments on the flow past circular cylinder at low Reynolds number. J. Fluid Mech. **6**, 547–567 (1959)
33. VDI-Gesellschaft: VDI-Wärmeatlas, 10th edn. Springer, Düsseldorf (2006)
34. Ribe, N.M., Huppert, H.E., Hallworth, M.A., Habibi, M., Bonn, D.: Multiple coexisting states of liquid rope coiling. J. Fluid Mech. **555**, 275–297 (2006)
35. Ferziger, J.H., Perić, M.: Computational Methods for Fluid Dynamics, 3rd edn. Springer, Berlin (2002)
36. Zdravkovich, M.M.: Flow Around Circular Cylinders, Vol 1: Fundamentals. Oxford University Press, New York (1997)
37. Marheineke, N., Wegener, R.: Fiber dynamics in turbulent flows: General modeling framework. SIAM J. Appl. Math. **66**(5), 1703–1726 (2006)
38. Hoerner, S.F.: Fluid-dynamic Drag. Practical Information on Aerodynamic Drag and Hydrodynamic Resistance. Published by the author. Obtainable from ISVA (1965)
39. Mahadevan, L., Keller, J.B.: Coiling of flexible ropes. Proc. R. Soc., Math. Phys. Eng. Sci. **452**, 1679–1694 (1996)
40. Marheineke, N., Wegener, R.: Fiber dynamics in turbulent flows: specific Taylor drag. SIAM J. Appl. Math. **68**, 1–23 (2007)